PAPER

Check for updates

Formation of antireflection Zn/ZnO core–shell nano-pyramidal arrays by O2+ ion bombardment of Zn surfaces

Noelia Benito,[a] Gonzalo Recio-Sánchez,[b] Ramón Escobar-Galindo†[c] and Carlos Palacio [ID] *[a]

ZnO is probably one of the most studied oxides since ZnO nanostructures are a very rich family of nano-materials with a broad variety of technological applications. Although several chemical techniques offer the possibility to obtain such ZnO nanostructures, here we show that the controlled modification of the zinc surface by low-energy O2+ bombardment leads to the formation of core–shell Zn/ZnO nano-pyramidal arrays that suppress the reflection of light decreasing the reflectivity below 6% in the wave-length range of 300–900 nm. This controlled and scalable protocol opens the door to a broad range of possibilities for the use of ion bombardment to produce surface modifications for technological applications in the field of photoelectric devices and solar cells.

Introduction

Nanostructures are widely used in electronic and opto-electronic nanodevices since they improve the properties of the devices with respect to the direct use of thin films. In this respect, it is well known that sub-wavelength structures (SWSs) can improve the optical and absorptive properties of the solar cells due to an intrinsic antireflection effect.[1] It has been demonstrated theoretically and experimentally[2,3] that reflectance can be decreased by placing nanowires on a surface instead of using the thin film counterpart, and, more importantly, the reflectance can be tuned by changing the filling ratios (diameter of the nanowire/distance between them). A plausible explanation of this phenomenon is based on the fact that the optical properties of nanowire layers are mainly determined by the diffuse multiple scattering of light. In these applications based on nanostructures, ZnO plays an important role since it can display a whole family of nanostructures where different morphologies and orders, from random distri-bution to biomimetic forms as moth-eye structures, induce different properties in the nanomaterials.[4–6]

Low-energy ion bombardment is a useful tool to generate controlled chemical modifications of the surface as well as ordered nanostructures.[7–12] However, the fabrication of ZnO nanostructures has been carried out up to now using different physical and chemical classical methods such as hydrothermal synthesis,[4] sol–gel,[1] LP-CVD,[13] sputtering,[14] thermal evapo-ration,[15] *etc.*, most of them increasing the temperature up to 500 °C and no attempt has been made to develop such nano-structures using ion bombardment methods. In this context we demonstrate that, under the appropriate conditions, a con-trolled modification of the zinc surface by low-energy O2+ bom-bardment leads to the formation of Zn/ZnO nano-pyramidal arrays that strongly suppress the reflection of light in the wave-length range from the ultraviolet to the near infrared region. In fact, the antireflection properties can be controlled through the ion fluence. These findings enormously increase the range of possibilities for using reactive low energy ion bombardment to produce surface modifications for optical technologies.

Experimental methods

The Zn/ZnO nano-pyramidal arrays have been prepared by O2+ bombardment of metallic Zn foil (99.9% purity) provided by MaTecK GmbH. Substrates were introduced into an ultra-high vacuum (UHV) preparation chamber next to the main analysis chamber both at a base pressure in the range of 10^{-10} mbar. The oxygen bombardment was carried out at 3 keV at a pressure of 2×10^{-4} mbar and keeping the substrate at room temperature. The ion beam current density, measured with a

*[a]Departamento de Física Aplicada, Facultad de Ciencias,
Módulo 12. Universidad Autónoma de Madrid, Cantoblanco, 28049-Madrid, Spain.
E-mail: carlos.palacio@uam.es*
*[b]Núcleo de Bioproductos y Materiales Avanzados, Facultad de Ingeniería,
Universidad Católica de Temuco, Temuco, 4781509, Chile*
*[c]Instituto de Ciencia de Materiales de Madrid (ICMM(CSIC)), Cantoblanco,
28049-Madrid, Spain*
†Present address: Abengoa Research S. L., Abengoa, Seville, Campus Palmas
Altas 41014, Spain.

Faraday cup that can be placed in the same position as the sample holder, was 0.021 mA cm^{-2}. These experimental conditions lead to an ion beam with a flat profile greater than ~1 cm × 1 cm. The angle between the surface normal and the ion beam was 0°. The fluence was increased sequentially from 0 to 3.9×10^{18} ions per cm^2 in six steps. After every step the substrate was analysed "*in situ*" by X-ray photoelectron spectroscopy (XPS) and Auger electron spectroscopy (AES) and, "*ex situ*" by atomic force microscopy (AFM), field emission scanning electron microscopy (FESEM), X-ray diffraction (XRD) and UV-visible spectrometry. The XPS and AES spectra were recorded using a hemispherical analyzer (SPECS Phobios 100MDC-5). The pass energy was 9 eV, giving a constant resolution of 0.9 eV. The Au 4f$_{7/2}$ at 84.0 eV, Ag 3d$_{5/2}$ at 368.3 eV and Cu 2p$_{3/2}$ at 932.7 eV lines of reference samples were used to calibrate the binding energies. A twin anode (Al–Mg) X-ray source was operated at a constant power of 300 W, using Mg Kα (1253.6 eV) radiation. All the spectra are presented after background subtraction based on a modified Shirley method.[16]

The morphology of the samples was characterized by atomic force microscopy in air (AFM, Nanotec) using a SiN OLYMPUS Micro Cantilevers RC800PSA with a pyramidal shape of 2.9 μm height and a tip radius of ~15 nm in tapping mode, the size of the analysed area being 5 × 5 μm, and by field emission scanning electron microscopy (FESEM, Philips XL30 S-FEG). The crystal structures of the samples have been investigated by X-ray diffraction (XRD) using a diffractometer Siemens D5000 equipped with a Si–Li detector (SolX, Bruker) and an X'Pert PRO high-resolution diffractometer operating with the α1 configuration (Cu Kα1 radiation) for grazing incidence diffraction (GIXRD).

The reflectance spectra of the bombarded substrates and Zn foil were obtained on a double-beam spectrophotometer with a double monochromator (Jasco V-560) operating in the wavelength range of 300–900 nm with a scanning speed of 10 nm s^{-1}.

Results and discussion

Fig. 1(a–f) show the AFM images of the Zn surface bombarded with O$_2^+$ with an ion energy of 3 keV, under normal incidence and at room temperature. The fluence was increased sequentially from (a) to (f); (a) 4.4×10^{17} ions per cm^2, (b) 8.9×10^{17} ions per cm^2, (c) 1.3×10^{18} ions per cm^2, (d) 2.2×10^{18} ions per cm^2, (e) 3.0×10^{18} ions per cm^2 and (f) 3.9×10^{18} ions per cm^2. In addition to that, the tilted views of the FESEM images obtained for (a) 2.2×10^{18} ions per cm^2, (b) 3.9×10^{18} ions per cm^2 (near the centre of the sample) and (c) 3.9×10^{18} ions per cm^2 (near the edge of the sample) are also shown in Fig. 2. Both figures illustrate that the development of a morphology of homogeneous and random rod arrays with tapered pyramidal tops and no long-range order is observed. Specifically, Fig. 1 shows that the height and width of such nanostructures increases with increasing the fluence and can reach maximum values above 1 μm in both cases.
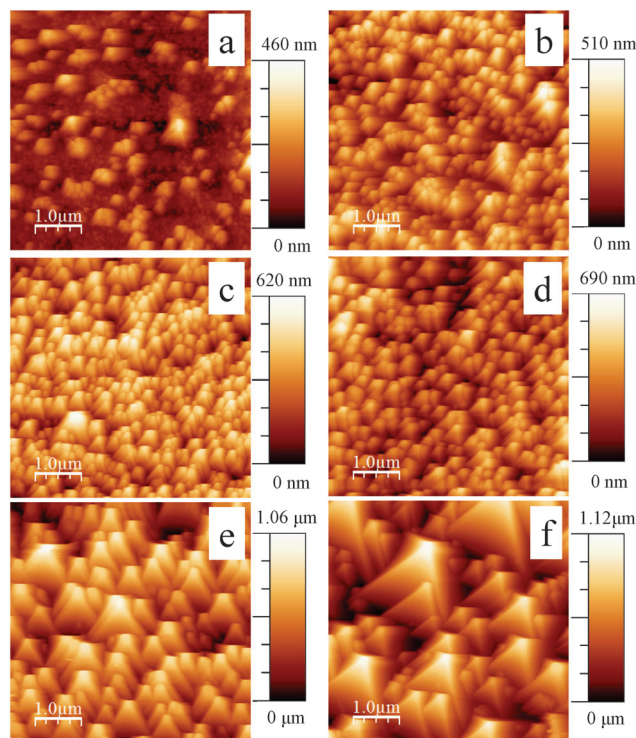
Fig. 1 AFM images of Zn foil bombarded with O$_2^+$ at 3 keV and normal incidence using different fluences as explained in the text. The lateral scale is the same for all images. The vertical scale increases from (a) to (f).

Further insight into the pyramid formation and growth mechanisms can be obtained by analysing the density of pyramids. Fig. 3 shows the measured density of pyramids (full squares) as a function of the fluence. As can be observed, the results of Fig. 3 point to a two stage mechanism for the growth of the rod array. Both, Fig. 1 and 3, show that the density and height of the pyramids increase with increasing fluence, up to around 1.3×10^{18} ions per cm^2 (first stage). Above this fluence (second stage), a decrease in the density of pyramids is observed along with an increase in their height and width and a more defined shape.

With the aim of understanding the growth mechanisms of the ZnO nanostructures, we have carried out numerical simulations using Monte Carlo (MC) procedures involving two stages for the growth of the pyramidal array. For simplicity, we assumed that the analysed surfaces of 5 μm × 5 μm (Fig. 1) can be represented by a square lattice of 39 × 39 points. A point of the lattice is selected at random and then each point can be randomly occupied by a rod (an event) with a probability p [$0 \leq p \leq 1$] (or it is empty with a probability $1 - p$). Every time a position is occupied, we look for the existence of an occupied first neighbor. If this is the case, the height growth of the rod is allowed (an arbitrary unit) instead of allowing the lateral growth of the rod when we have two occupied first neighbor positions as in the case of percolation structures. This represents the nanostructure nucleation stage. The value of p necessary to obtain the maximum rod density is
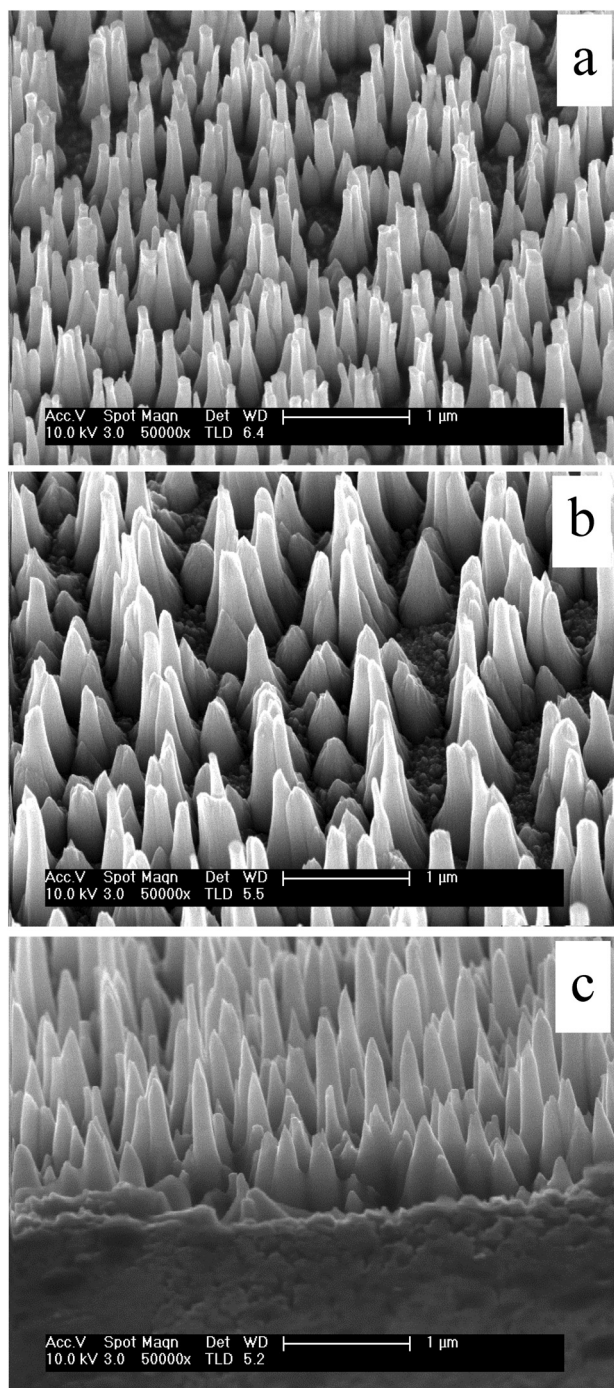
Fig. 2 Tilted view of the FESEM images obtained for (a) 2.2×10^{18} ions per cm^2, (b) 3.9×10^{18} ions per cm^2 near the center of the sample and (c) 3.9×10^{18} ions per cm^2 near the edge of the sample.

Fig. 3 Experimental density of pyramids (full squares) as a function of the fluence. The red down triangles represent the density of pyramids derived from the MC simulation. The growth of the nanostructures is clearly divided into two different stages.

pyramid and its neighbors is allowed with the same probability (a new event). The results of the MC simulation are given in Fig. 4, as height maps, for a different number of events (the number of events in the MC simulation is related to the fluence in the real experiment). As can be observed, these results correlate well to the AFM images of Fig. 1. In addition to this, the density of pyramids has been plotted in Fig. 3 (red down triangles) as a function of the number of events. Dotted and dashed lines have been included to guide the eye. Again,

Fig. 4 Height maps of the nanostructure growth, simulated using MC methods, for a different number of events (see the text), (a) 150, (b) 1000, (c) 4500 and (d) 1×10^{8}. The height scale is normalized to the maximum height.

0.19, Fig. 3, this is, obviously, smaller than the percolation threshold (p_c = 0.6) in percolating systems.[17] Once this condition is fulfilled, the lateral growth of the existing pyramids is simulated (second stage) allowing diffusion-like processes to the first neighbors. In such a case, a random point of the square lattice is chosen, if this position is occupied then the highest neighbor is looked for and the height growth of this
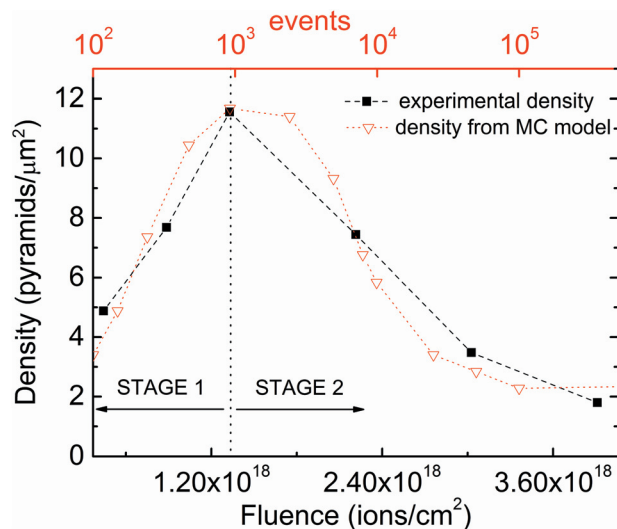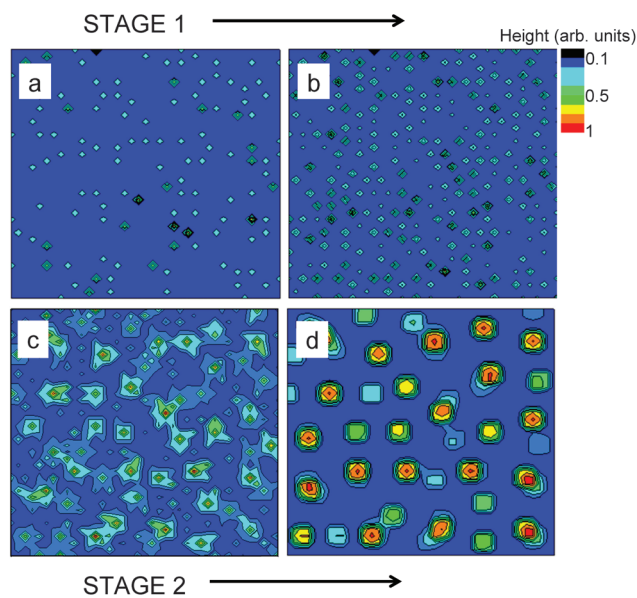
good agreement between the experimental results and the simulation is observed, therefore supporting the validity of the proposed model.

As will be explained later, another important issue related to the reflectivity of the surfaces is the height of the nanostructures. Fig. 5(a) shows the distribution of heights for the pyramidal nanostructures of Fig. 1(d) corresponding to the maximum density of pyramids (see also Fig. 3) and Fig. 5(b) shows the distribution of heights for the MC simulated nanostructures of Fig. 4(b) which also corresponds to the maximum density of the simulated nanostructures. Both are Gaussian distributions (continuous red lines), the experimental one is centered at 470 nm and its full width at half maximum is 162 nm. The height of the simulated nanostructures is given in arbitrary units normalized to the maximum height, and the linear relationship between both scales is given on the top of Fig. 5(b). As can be observed, there is perfect agreement between both results, therefore indicating that the proposed MC simulation model for the nanostructure formation and growth is able not only to correctly reproduce the density of the nanostructures, but also their distribution of heights.

According to the model put forward by K. W. Pierson et al.,[18] the preferential sputtering and the formation of "seed" cones/pyramids should be the two main mechanisms responsible for the development of the surface topography found on our samples. Initially, for a flat surface, the sputtering yield should be that of Zn (5.7 atoms per ion, calculated using the SRIM software package[19]). For low ion fluences, oxide islands would nucleate randomly as a consequence of the chemical reaction between oxygen and the Zn substrate as happens for the chemical reaction of oxygen with other metal surfaces.[20] Oxide nuclei have a lower total sputtering yield (4 atoms per ion) than the substrate and then, with increasing fluence, the Zn substrate will erode faster than the oxide nuclei resulting in

the formation of a roughened surface topography leading to cone/pyramid-like structures that grow by surface diffusion. This surface will now alter the original angular distribution of the ejected atoms with respect to the surface normal. When the aspect ratio of the formed nanostructures, defined as the ratio of the height to the nanostructure width, is greater than 0.5 [18] (in our case the aspect ratio is >1 for fluences above 4.4 × 10^{17} ions per cm^2), the total sputtering yield may be indeed lowered due to the re-deposition "shadowing effect".[18] Also, it should be noted that Wehner[21] showed that the seed cone mechanism occurs not only for seed materials with a lower sputtering yield but also for those with a higher melting point (T_M) than the substrate material as in the case of ZnO (T_M = 1975 °C)[22] compared to Zn (T_M = 419.5 °C).[22] The theoretical basis of the model was previously developed by R.M. Bradley[23] and it was used to explain the nanostructures reported in semiconductors as InSb and InP during Ar$^+$ bombardment.[24] It should be indicated that the above-mentioned mechanisms are fully consistent with the phenomenological MC model proposed above to reproduce our experimental results. In addition to this, it is important to note that a rough estimation of the mean eroded depth during ion bombardment using the atomic volume of Zn, the sputtering yield calculated from SRIM (5.7 atoms per ion)[19] and the primary ion current density gives a value of ~3.5 µm for the highest fluence used in this work (3.9 × 10^{18} ions per cm^2), therefore indicating that the tips of the pyramids are far away from the original pristine surface.

Further information on the morphology and chemistry of the formed nanostructures can be obtained using XRD, XPS and AES. Fig. 6 shows the GIXRD pattern of the heavily bombarded Zn surface (3.9 × 10^{18} ions per cm^2). In addition to this, the GIXRD pattern for the Zn substrate (Zn foil) is also given for comparison. From Fig. 6 we can see that the main
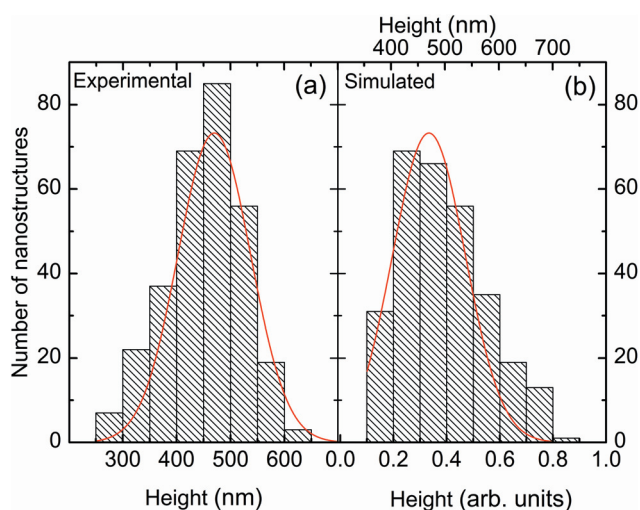

Fig. 5 (a) Distribution of heights for the pyramidal nanostructures of Fig. 1(d) and (b) distribution of heights for the MC simulated nanostructures of Fig. 4(b). Both cases correspond to the maximum density of nanostructures.
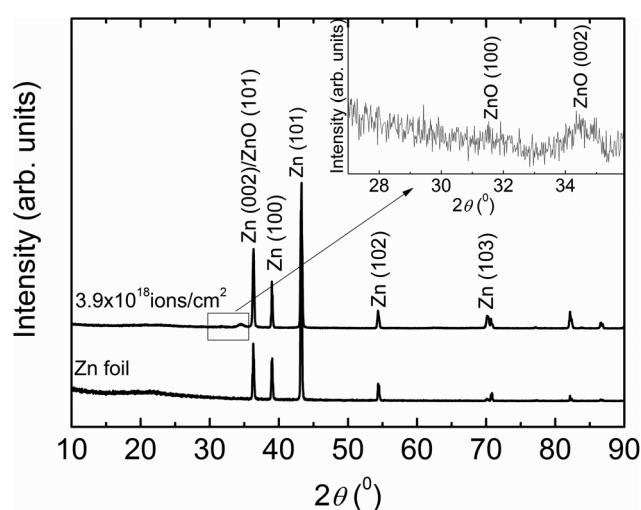

Fig. 6 GIXRD spectrum of the heavily bombarded Zn surface (3.9 × 10^{18} ions per cm^2). The spectrum corresponding to the clean Zn substrate (Zn foil) is also given for comparison. The inset shows a zoom image of the indicated region.

peaks in the XRD spectrum of pure Zn correspond to polycrystalline Zn with a hexagonal close packed crystal lattice.[25] As we bombard the sample, the XRD spectra show a mixed pattern involving Zn and ZnO peaks[25,26] which are weaker and broader than the metallic ones and are visible for high fluences at $2\theta \approx 34.4°$ (see the inset), which corresponds to the (002) direction of the hexagonal ZnO structure. A peak should appear at $2\theta \approx 31.7°$ corresponding to the (100) direction but it is blurred by the noise. The peak at $2\theta \approx 36.2°$ corresponds to the overlap of the Zn (002) and ZnO (101) directions. The broadening of the ZnO peaks should be attributed to crystal lattice distortions and structural defects produced during ion bombardment. As we will discuss later on the basis of AES results, the presence of ZnO peaks is related to the existence of a very thin ZnO film covering the nanostructures.

Complementary information on the chemistry and thickness of the film can be obtained using XPS and AES. It should be pointed out that the variations of the Zn $2p_{3/2}$ peak associated with the oxidation during O_2^+ bombardment are very weak (only a small shift of around -0.4 eV and a FWHM increase of around 20% with respect to the clean Zn surface). Therefore, Zn Auger spectra have been used to analyse the chemical changes appearing during oxygen bombardment. Fig. 7 shows the change in the Zn $L_3M_{45}M_{45}$ X-ray excited AES spectra observed during O_2^+ bombardment (left side). The sequence of the fluence variation from (a) to (f) has been described above. The AES spectra of clean Zn and ZnO are also included for comparison. The doublet at around 992 eV and 994.8 eV is due to the Zn^0 metallic state whereas that at 987.5 eV and 990.6 eV is attributed to the oxidized Zn (Zn^{2+} state) in good agreement with the previously published results on the initial oxidation of Zn.[27] It should be indicated that the metallic features are clearly observed for all fluences. Since the probed depth is roughly three times the attenuation length of the $L_3M_{45}M_{45}$ electrons ($\lambda = 1.2$ nm (ref. 28)), the thickness of the oxide film formed on the nanostructures

should be around 3λ, that is, 3.6 nm thick, which is in good agreement with the ion range calculated using the SRIM software package[19] ($R_p = 3.9$ nm), indicating again the formation of core–shell nanostructures covered by a very thin ZnO film.

Fig. 7 also shows the change in the O 1s XPS spectra observed during O_2^+ bombardment (right side) for the same sequence of the fluence variation. Two components (dashed lines) are clearly identified at 530.5 eV and 532.2 eV. The lower BE peak is commonly attributed to the oxide,[29,30] however the origin of the other peak is still controversial. It has been attributed to OH species,[29,30] contaminant surface species[29,30] and oxygen-defect sites related to oxygen atom vacancies in the matrix.[31] It should be indicated that (a) combined XPS and HREELS experiments show the presence of the high BE component even in the absence of the characteristic vibration of OH stretching[30,32] and (b) in our case, XPS survey spectra do not show other species different from Zn and oxygen. Therefore, considering that ion bombardment is well known to generate surface defects,[12] we attribute the higher BE peak to oxygen-defect sites related to oxygen atom vacancies in the near surface.

An amazing consequence of the ion bombardment is the colour changes observed on the zinc surface from grey for the clean surface to dark black for the heavily bombarded surface. Fig. 8(a) shows two photographs, one of the Zn metallic surface (left side) and the other one of a heavily bombarded surface using an ion fluence of 2.2×10^{18} ions per cm^2 (right side). As we will see below, this phenomenon is attributed to the reflectivity suppression by the nano-pyramidal arrays. In addition to this, Fig. 8(b) shows the reflectance spectra obtained from 300 to 900 nm wavelengths for three different fluences. The reflectance spectrum for the zinc surface is also given for comparison. As can be observed, the reflectance can be controlled through the fluence and, for higher fluences, is lower than 6% in the measured wavelength interval whereas the reflectance of the Zn foil is around 55% within the same interval, therefore indicating a strong suppression of the surface reflectivity from the ultraviolet to the near-infrared part of the spectrum, due to the nanostructures developed during O_2^+ bombardment. These figures are similar to the results found by Y. Tian et al.[4] on ZnO nanostructures grown by hydrothermal methods.

Using patterns similar to the moth eyes, synthetic anti-reflection surfaces have been simulated. According to the previous published analysis of such patterns, on a scale below the wavelength of incident light, the array of tapered nanostructures should produce a gradual transition of the refractive index leading to a reduction of the reflection over a large range of wavelengths and angles of incidence. The periodicity, the nanostructure diameter and the height were found to be the key parameters in this reduction.[4,33,34]

Antireflection surfaces have been modeled according to the conical geometry of the inset in Fig. 8(c), solving Maxwell's equations for the above-mentioned geometry. A commercial-grade simulator LUMERICAL[35] based on the finite-difference time-domain method was used to perform the calculations.
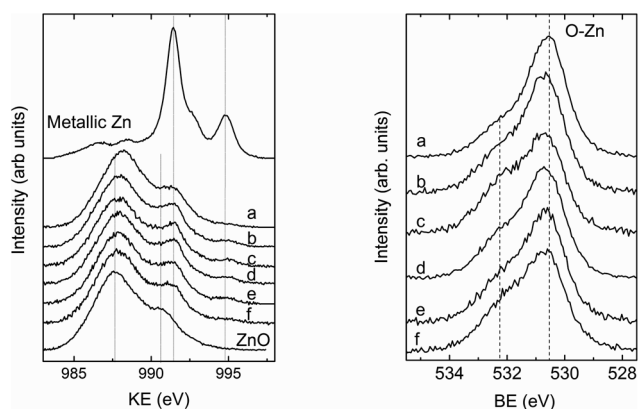
Fig. 7 Zn $L_3M_{45}M_{45}$ X-ray excited AES spectra obtained during O_2^+ bombardment (left side) and O 1s XPS spectra (right side) for the same sequence of fluence variation. The sequence for the fluence variation from (a) to (f) is explained in the text.
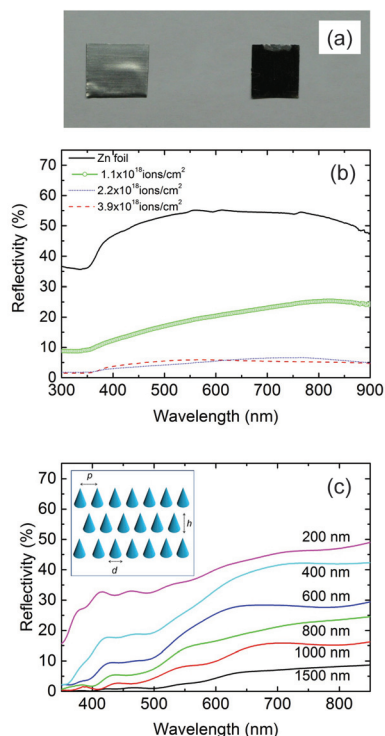
Fig. 8 (a) Optical photograph of the Zn metallic surface (left side) and the heavily bombarded surface using an ion fluence of 2.2 × 10^18 ions per cm² (right side) (b) reflectance spectra obtained for three different fluences. The spectrum corresponding to the clean Zn substrate (Zn foil) is also given for comparison. The maximum height of the nanostructures varies from 620 nm to 1120 nm (see Fig. 1) as the fluence increases. (c) Calculated reflectance spectra for the pattern given in the inset, with d = 200 nm, p = 300 nm and h varying in the range of 200–1500 nm.

Conclusions

To summarize, we show here that the reactive ion bombardment of metallic surfaces can lead to more complex situations than that previously reported. In particular, the controlled bombardment of zinc surfaces with low energy O_2^+ leads to the formation of core–shell ZnO nano-pyramidal arrays that suppress the reflection of light decreasing the surface reflectivity below 6% in the wavelength range of 300–900 nm. Such nanostructures are homogeneously distributed on the surface, display a normal distribution of heights, and are covered by a very thin ZnO film. These findings open the door to a broad range of possibilities to produce surface modifications using reactive low-energy ion bombardment which can be used for technological applications as for antireflection materials for solar energy devices.

Conflicts of interest

There are no conflicts of interest to declare.

Acknowledgements

Here, d stands for the rod diameter, p the periodicity and h the nanostructure height. Fig. 8(c) shows the simulated reflectance spectra for the above-mentioned geometry with d = 200 nm, p = 300 nm and h varying in the range of 200–1500 nm. The results from our calculations show that the modeled nanostructures exhibit a decrease in the reflectivity upon increasing the height. Similar calculations (not shown) by keeping d and h constant and varying the periodicity p in the range of 200–400 nm show that the reflectance of the nanostructures strongly decreases below 5% with decreasing periodicity. It should be pointed out that the experimental data of Fig. 1 display a Gaussian distribution of the base sizes and also for the heights of the nanostructures (see also Fig. 5) instead of constant values and no short-range order is observed (the average separation of the nanostructures is ~300 nm). Nevertheless, the comparison of the simulated reflectance spectra of Fig. 8(c) with the experimental spectra of Fig. 8(b) shows good agreement displaying in both cases the same reflectivity decrease with increasing nanostructure heights. These results point to the nanostructure height as the main parameter responsible for the antireflection properties of the bombarded surfaces, which can be easily controlled by the ion fluence.

Notes and references

1 J. Y. Chen and K. W. Sun, *Sol. Energy Mater. Sol. Cells*, 2010, **94**, 930–934.
2 L. Hu and G. Chen, *Nano Lett.*, 2007, **7**, 3249–3252.
3 O. L. Muskens, J. Gómez Rivas, R. E. Algra, E. P. A. M. Bakkers and A. Lagendijk, *Nano Lett.*, 2008, **8**, 2638–2642.
4 Y. Tian, C. Hu, Y. Xiong, B. Wan, C. Xia, X. He and H. Liu, *J. Phys. Chem. C*, 2010, **114**, 10265–10269.
5 Y. Chao, C. Chen, C. Lin, Y. Dai and J. He, *J. Mater. Chem.*, 2010, **20**, 8134–8138.
6 B. Shin, T. Lee, J. Xiong, C. Hwang, G. Noh, J. Cho and J. Myoung, *Sol. Energy Mater. Sol. Cells*, 2011, **95**, 2650–2654.
7 N. Benito and C. Palacio, *Appl. Surf. Sci.*, 2015, **351**, 753–759.
8 N. Benito and C. Palacio, *J. Phys. D: Appl. Phys.*, 2014, **47**, 015308.
9 C. Palacio, J. Olvera, J. L. Plaza and E. Diéguez, *Surf. Coat. Technol.*, 2012, **206**, 3146–3150.
10 S. Facsko, T. Bobek, H. Kurz, T. Dekorsy, S. Kyrsta and R. Cremer, *Appl. Phys. Lett.*, 2002, **80**, 130–132.

11 R. Gago, L. Vázquez, R. Cuerno, M. Varela, C. Ballesteros and J. M. Albella, *Appl. Phys. Lett.*, 2001, **78**, 3316–3318.

12 B. M. Pabón, J. I. Beltrán, G. Sánchez-Santolino, I. Palacio, J. López-Sánchez, J. Rubio-Zuazo, J. M. Rojo, P. Ferrer, A. Mascaraque, M. C. Muñoz, M. Varela, G. R. Castro and O. Rodríguez de la Fuente, *Nat. Commun.*, 2015, **6**, 6147.

13 C. Battaglia, J. Escarré, K. Söderström, M. Charrière, M. Despeisse, F. Haug and C. Ballif, *Nat. Photonics*, 2011, **5**, 535–538.

14 S. Kim, M. Jeong, B. Oh, W. Lee and J. Myoung, *J. Cryst. Growth*, 2006, **290**, 485–489.

15 Q. Zhao, X. Y. Xu, X. F. Song, X. Z. Zhang, D. P. Yu, C. P. Li and L. Guo, *Appl. Phys. Lett.*, 2006, **88**, 033102.

16 D. A. Shirley, *Phys. Rev. B: Solid State*, 1972, **5**, 4709–4714.

17 D. W. Heermann, *Computer simulation methods in theoretical physics*, Springer, Berlin, Heidelberg, 1986.

18 K. W. Pierson, J. L. Reeves, T. D. Krueger, C. D. Hawes and C. B. Cooper, *Nucl. Instrum. Methods Phys. Res., Sect. B*, 1996, **108**, 290–299.

19 J. F. Ziegler, M. D. Ziegler and J. P. Biersack, *Nucl. Instrum. Methods Phys. Res., Sect. B*, 2010, **268**, 1818–1823.

20 C. Palacio, H. J. Mathieu and D. Landolt, *Surf. Sci.*, 1987, **182**, 41–55.

21 G. K. Wehner, *J. Vac. Sci. Technol., A*, 1985, **3**, 1821–1835.

22 *Handbook of Chemistry and Physics*, ed. D. R. Lide, CRC Press, Boca Raton, 84th edn, 2003.

23 R. M. Bradley and J. M. E. Harper, *J. Vac. Sci. Technol., A*, 1988, **6**, 2390–2395.

24 M. Szymonski, F. Krok, P. Struski, J. Kolodziej and B. Such, *Prog. Surf. Sci.*, 2003, **74**, 331–341.

25 Joint Committee on Powder Diffraction Standards, Powder Diffraction File No 036-1451 (ZnO) and #00-004-0831 (Zn).

26 O. Lupan, L. Chow, G. Chai and H. Heinrich, *Chem. Phys. Lett.*, 2008, **465**, 249–253.

27 M. Xue, Q. Guo, K. Wu and J. Guo, *Langmuir*, 2008, **24**, 8760–8764.

28 S. Tanuma, C. J. Powell and C. R. Penn, *Surf. Interface Anal.*, 1994, **21**, 165–176.

29 J. C. Dupin, D. Gonbeau, P. Vinatier and A. Levasseur, *Phys. Chem. Chem. Phys.*, 2000, **2**, 1319–1324.

30 F. Wiame, F. R. Jasnot, J. Światowska, A. Seyeux, F. Bertran, P. Le Fèvre, A. Taleb-Ibrahimi, V. Maurice and P. Marcus, *Surf. Sci.*, 2015, **641**, 51–59.

31 Q. Bao, X. Liu, Y. Xia, F. Gao, L. D. Kauffmann, O. Margeat, J. Ackermann and M. Fahlman, *J. Mater. Chem. A*, 2014, **2**, 17676–17682.

32 S. Maroie, P. A. Thiry, R. Caudano and J. J. Verbist, *Surf. Sci.*, 1983, **127**, 200.

33 J. Zhu, Z. Yu, G. F. Burkhard, C. M. Hsu, S. T. Connor, Y. Xu, Q. Wang, M. McGehee, S. Fan and Y. Cui, *Nano Lett.*, 2009, **9**, 279–282.

34 S. A. Boden and D. M. Bagnall, *Appl. Phys. Lett.*, 2008, **93**, 133108.

35 Lumerical Solutions, Inc. http://www.lumerical.com/tcad-products/fdtd/.